J. Electrochem. Sci. Eng. **14(4)** (2024) 499-522; http://dx.doi.org/10.5599/jese.2246

Open Access : : ISSN 1847-9286
https://pub.iapchem.org/ojs/index.php/JESE

Original scientific paper

High-velocity oxy-fuel and high-velocity air fuel sprayed WC-Co-Cr coatings on solution-treated 21-4N steel for slurry and corrosion resistance

Rajanna Lingappa[1,✉], Tumakur Gangadhar Mamatha[1], Momballi Shivappadevaru Prabhuswamy[2], Vikrant Singh[3] and Anuj Bansal[3]

[1]*Department of Mechanical Engineering, JSS Science and Technology University, Mysuru, Karnataka 570006, India,*
[2]*Department of Mechanical Engineering, JSS Academy of Technical Education, Noida, Uttar Pradesh 201301, India*
[3]*Department of Mechanical Engineering, Sant Longowal Institute of Engineering and Technology, Longowal, Sangrur-148106, Punjab, India*

Corresponding author: ✉rajannalingappa07@gmail.com

Received: January 13, 2024; Accepted: April 19, 2024; Published: April 23, 2024

Abstract

This study aims to fabricate WC-Co-Cr coatings on the solution-treated 21-4N steel utilizing high-velocity oxy-fuel (HVOF) and high-velocity air fuel (HVAF) techniques. The microstructure, hardness, surface quality, porosity, slurry erosion, and corrosion resistance of HVOF and HVAF coatings on solution-treated 21-4N steel were investigated and compared. The HVAF sprayed WC-Co-Cr coating exhibited dense structure, more hardness (1582 HV), greater fracture toughness (5.69 MPa $m^{1/2}$), less decarburization, and lower porosity (0.97 %) as compared to HVOF sprayed coating. Further, slurry jet erosion tests and electrochemical corrosion tests provide a comprehensive evaluation of the coating's performance under erosive and corrosive conditions. Eventually, the conclusive results of the study affirm the exceptional performance of the high-velocity air fuel sprayed WC-Co-Cr coating, demonstrating its superiority in both erosion and corrosion resistance compared to the high-velocity oxygen fuel sprayed coating.

Keywords

Slurry jet erosion test, electrochemical corrosion test, surface modification

Introduction

Slurry erosion is a significant concern in various industries where mechanical components operate in harsh conditions, such as slurry pumps, chemical processing equipment, hydropower machinery, and construction equipment [1]. Slurry erosion is a form of wear caused by the abrasive action of a mixture of solid particles suspended in a liquid (water). Slurry erosion emerges when

abrasive particles suspended in a liquid come into contact with the surfaces of in-service components. This abrasive interaction leads to material loss and degradation of the affected components over time. By taking a proactive approach to protecting components against slurry wear and implementing appropriate measures, we can significantly extend their lifespan and reduce the maintenance and replacement costs of industrial and mechanical systems. Therefore, surface coatings and the use of wear-resistant metals and alloys are crucial techniques in engineering and material science for enhancing the durability and longevity of mechanical components, especially in harsh environments. Several surface modification processes, including weld overlays, chemically and thermally diffused coatings, and thermal spray processes, have been widely utilized to develop wear-resistant coatings on various components in industries where abrasion and erosion are prevalent concerns [2]. Thermal spray coatings have gained significant popularity in recent years due to their flexibility in material selection, minimal impact on coating properties, cost-effectiveness, lightweight, adaptability to complex shapes, rapid application process, versatility across industries, long service life, and outstanding resistance to erosive and corrosive wear [3]. However, WC-Co-Cr composite coatings were practically proven and precisely engineered compositions, enabling the development of coatings tailored for erosive wear and corrosion environments [4]. WC-Co-Cr coatings produced by the high-velocity oxy-fuel (HVOF) technique possess an optimum combination of high levels of hardness, wear, and corrosion resistance, making them suitable for a wide range of applications in industries such as aerospace, oil and gas, and hydropower. However, prolonged exposure of powder particles to the high-temperature flame in the HVOF process can lead to decarburization. As a result, the formation of undesired phases like W_2C and amorphous phases can have a detrimental effect on the quality and performance of HVOF-processed cermet coatings, impacting their resistance to erosive and corrosive wear [5]. Therefore, minimizing decarburization is a crucial aspect of enhancing the resistance of coatings (WC-Co-Cr) to both corrosion and erosion wear. Hence, the high-velocity air fuel (HVAF) process has gained recognition for its effectiveness in limiting decarburization during the spraying of coatings, particularly when compared to other thermal spray processes like HVOF. The HVAF process is a thermal spray coating technique that involves the controlled combustion of a mixture of air and fuel gas, usually propane or hydrogen, to produce a high-velocity, high-temperature gas stream used to propel coating material onto a substrate. The lower combustion temperature of HVAF compared to HVOF results in less prolonged exposure of the powder particles to high temperatures, thereby minimizing the extent of decarburization [6]. Therefore, the HVAF process is a preferred choice in situations where minimizing decarburization and achieving specific mechanical properties like high hardness, low porosity, uniformity, and higher fracture toughness are critical factors for the application. According to various researchers, improved coating properties are essential for enhancing resistance to erosive and corrosive wear [7-9]. Furthermore, extensive research has been conducted to analyze the structure and tribological properties of WC-Co-Cr coatings deposited through HVOF and HVAF processes [10-12]. Liu *et al.* [13] investigated the slurry erosion resistance of AISI 304 steel coated with a combination of WC-Co-Cr powder and Nano WC-12Co powder. They reported that the addition of 15 % WC-12Co nanopowder to the conventional WC-Co-Cr powder resulted in a significant improvement in coating hardness (1677 to 1873 HV0.3). Due to the uniform distribution of nano-WC-12Co particles among WC particles, the structure is less porous and dense. The slurry erosion resistance of the coating with 15 % Nano WC-12Co added to the WC-Co-Cr was superior to that of the conventional HVAF sprayed WC-Co-Cr coating, attributed to enhanced hardness and fracture toughness. The study conducted by Wang *et al.* [14] performed wear and

corrosion studies on coatings produced using both HVOF/HVAF processes. HVOF coating exhibits a smaller degree of decarburization, whereas HVAF coating demonstrates no decarburization. They concluded that HVAF coating outperformed HVOF coating with wear and corrosion resistance owing to its higher hardness, lesser porosity, and better toughness. Wang *et al.* [15] conducted sand erosion and cavitation tests on WC-CoCr coatings that were deposited using both processes onto AISI 316 austenitic steel. The phase analysis by X-ray diffraction (XRD) indicated the presence of decarburization in the HVOF-sprayed coating. In contrast, the XRD analysis of the HVAF-sprayed coating showed no signs of decarburization and exhibited superior mechanical properties. The sand erosion with cavitation tests revealed that HVAF coating showed better wear resistance against HVOF coating owing to higher hardness, lower porosity, and better fracture toughness. Kumar *et al.* [16] performed a sand erosion experiment on the HVOF/HVAF fabricated coatings (WC-Co-Cr) on the underwater turbine steel (16Cr5Ni). HVAF coatings had lower erosion wear loss than HVOF coatings due to improved properties such as improved adhesion, increased toughness, heightened hardness, and greater residual stress with a lower level of oxidation. Yang Li *et al.* [17] conducted solid particle erosion tests on WC-Co-Cr coatings developed by HVOF/HVAF processes. Their investigation revealed that HVAF coatings exhibited superior erosion resistance compared to HVOF coatings across all tested angles owing to lesser porosity, high hardness, and improved fracture toughness. Another study conducted by Hong *et al.* [18] investigated the corrosion properties of WC-CoCr coatings fabricated by the HVOF process under various spray conditions to optimize coating porosity. They disclosed that the coating developed under a particular spray condition had improved corrosion resistance due to decreased porosity as compared to other coatings developed under different spray conditions. It's worth noting that while there's extensive research on the morphology, tribological properties, erosion, and corrosion studies of WC-Co-Cr coatings produced by HVOF and HVAF processes, there seems to be a gap in comparative studies specifically addressing the erosive and corrosive wear performance of coated thermally treated steel. This gap might present an opportunity for further research to explore and compare the erosive and corrosive wear performance of WC-Co-Cr coatings applied to thermally treated steel using both HVOF and HVAF methods. In addition, conducting focused studies on the erosion resistance of coatings and investigating the implications of various parameters is critical for advancing protective solutions in erosive environments. Thus, from all this literature, it can be said that the superior quality and consistency of HVOF coatings are emphasized and attributed to precise control over parameters such as particle velocity, temperature, and coating microstructure. Secondly, the enhanced adhesion of HVOF coatings to the substrate is underscored, resulting from stronger interfacial bonding and improved coating-substrate cohesion. Thirdly, the finer microstructures and superior mechanical properties of HVOF-sprayed coatings are highlighted, owing to the higher particle velocities and thermal energy associated with the HVOF process. Lastly, while acknowledging the cost-effectiveness of electric arc spray for certain applications, the overall performance and value of HVOF spraying in terms of coating quality and longevity are emphasized, considering factors such as reduced maintenance costs and extended service life of coated components.

By keeping the above-mentioned things in consideration, the current study aims to compare WC-10Co4Cr coatings fabricated using two different thermal spray processes, namely high-velocity oxygen fuel and high-velocity air fuel on the solution-treated 21-4N utilizing a similar feedstock powder. Various parameters, including cross-sectional microstructure, hardness, surface quality, fracture toughness, and porosity of the coatings, were evaluated and compared. Furthermore, two coatings were subjected to slurry wear and electrochemical corrosion tests to evaluate their

performance under erosive wear and in corrosive environments. In addition, the comparison is also based on the morphologies of the coatings produced by HVOF and HVAF methods, particularly tested under erosion and corrosion wear conditions.

Experimental

Substrate material and coating powder

Commercially available from H.C. Stark (sintered and dried), the 86WC-10Co-4Cr powder was deposited on the solution-treated 21-4N steel substrate by HVOF and HVAF thermal spray equipment. The chemical constituents of cast 21-4N steel are 0.5 % C, 20.8 % Cr, 3.6 % Ni, 8.8 % Mn, 0.33 % N, 0.25 % Si, 0.13 % Mo, 0.001 % S, 0.04 % P, and 65.549 % Fe. For the HVOF process, a coarse powder with a nominal particle size of 15 to 45 µm (AMPERIT 556.074) was used, whereas a fine powder with a nominal particle size of 5-30 µm (AMPERIT 556.059) was used for the HVAF process. The two feedstock powders employed had the same composition (5.073 wt.% C, 10.992 wt.% Co, 3.039 wt.% Cr and 80.896 wt.% W) with a mean particle size of 21 µm for HVOF and 19 µm for the HVAF process. Using a scanning electron microscope (SEM) allows for a detailed examination of the morphology and composition of the powder particles with the corresponding EDS plot shown in Figure 1. The EDS analysis represents the distinct elements like WC, Co, Cr, and C in the powders. Figure 1(a) depicts the powder that seems to exhibit a high degree of porosity but with ideal spherical shapes.

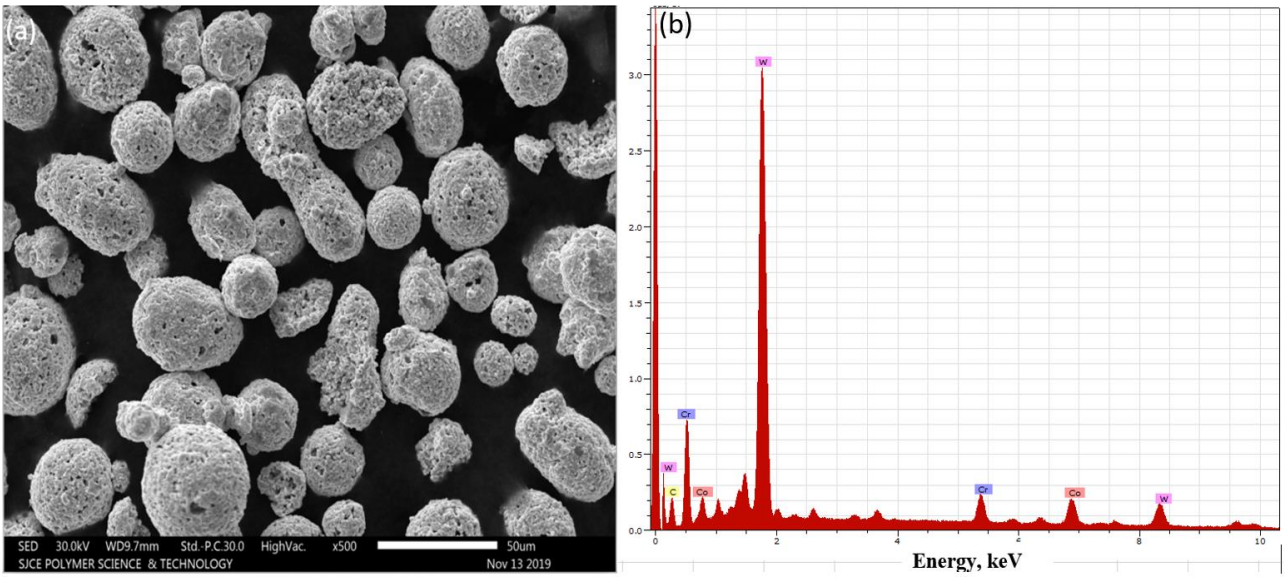

Figure 1. *Surface morphology of feedstock powder (a), and EDS graph (b)*

Coating procedure

Before coating deposition, a square specimen (100×100×5 mm^3) of solution-treated 21-4N steel was cleaned with acetone, and grit blasting was performed at 5 kg cm^{-2} pressure using alumina powder having a mesh size of 60 µm to enhance its roughness (R_a = 8.5 µm) for better adhesion of coating material. Two coating thicknesses of approximately 350 µm were developed using convertible gun C6 [Make: Kermetico] for both HVOF/HVAF systems at Spray Met Technologies Pvt. Ltd., Bengaluru, Karnataka. A square specimen sized 25×25×5 mm^3 [19] was machined from the coated substrate by a wire-electric discharge machine for a slurry erosion test. Table 1 provides the optimal process parameters used to develop the coatings. The temperature of the specimen was maintained below 120 °C during deposition by using a compressed air-cooling system, and the

spraying angle was 90 °C. Also, in the current research work, 2 levels and 3 factors are varied, keeping two parameters constant by varying one parameter at a time. So, the total samples coated from the HVOF and HVAF processes were 60 nos. (30 each). Each slurry experiment requires 3 samples, so a total of 18 from each HVOF and HVAF coated sample are consumed. Corrosion tests need 2 samples from each HVOF and HVAF coating.

Table 1 *HVOF and HVAF thermal spray process optimized process parameters with their values*

HVOF		HVAF	
Oxygen flow rate, SLPM*	250-300	Air flow rate, SLPM	83.4
Air flow rate, SLPM	460-550	Fuel (propane) bas flow rate, SLPM	84
Fuel (LPG) flow rate, SLPM	50-55	Nitrogen flow rate, SLPM	23.1
Oxygen pressure, MPa	1	H_2 flow rate, SLPM	15
Air pressure, MPa	5.5	Air pressure, MPa	5.79
Fuel pressure, MPa	7	Fuel pressure; MPa	5.92
Spray distance, mm	152-177	Spray distance, mm	177
Spray angle, °	90	Spray angle, °	90

*1 SLPM = 0.00073386 mol s^{-1}

Microstructure and phase characterization

Phase characterization of feedstock powder and fabricated coatings was conducted by employing a Bruker D8 Advance diffractometer (XRD) with an angular range of 2θ110 to 168° and an increment of 0.0001° angle using Cu Kα radiation. The field emission scanning electron microscope (FESEM) (ZEISS Neon 40) equipped with an energy dispersive spectroscopy (EDS) attachment was used to examine the coatings for microstructure cross-sections, the structure of feedstock powder, and the eroded sample surface. The roughness tester (Veeco Model: NT9100) was used to measure the surface irregularities of the fabricated coatings. Open-source image processing Image J analysis software was employed to determine the porosity of the as-sprayed coatings utilizing a 20,000× magnification SEM micrograph. The values reported were an average of ten measurements. The indentation crack method was used to measure the fracture toughness of the two coatings. The Vickers indenter was applied to the polished cross-section of the coating for 15 s at a load of 5 kg (49.05 N). The Evan and Wilsaw equation [20] was used to estimate the fracture toughness of coatings. The density of the coatings was calculated by subtracting the volume fractions of porosity from the volume fractions of their WC and Co-Cr binder counterparts. Carbide retention was calculated from the intensity integrals of WC and W_2C.

Microhardness of coatings

The Vickers microhardness test was conducted on various coated and uncoated samples employing the RMHT-201 apparatus. Indentation was executed under a load of 500 gm with a holding time of 20 seconds [21-22]. Subsequently, measurements were taken at five distinct points, and the average value was utilized for the analysis.

Slurry erosion wear test

According to the literature review, interacting factors comprising slurry velocity, impact angle, and sand concentration had noticeable effects on material removal [23]. The slurry erosion resistance of two separate thermally developed coatings was evaluated using a jet-type slurry erosion test apparatus, TR-411 [Ducom], as shown in Figure 2. The same test rig was also used by Singh *et al.* [24], in the existing literature. The test rig is made up of a conical-shaped tank (hopper) that can hold 60 kg of slurry. The slurry tank is filled with tap water and a particular size of sand

particles to prepare the slurry for testing. High-pressure fresh water is delivered into a mixing chamber through a positive displacement rotary vane pump powered by a 3-phase AC motor (1.5 kW). Furthermore, fresh sand particles are added into a mixing chamber using a spiral (worm) mechanism powered by an alternating current motor. Inside the mixing chamber, the freshly entered sand particles were mixed with high-pressure water before being ejected through a nozzle at the bottom of the mixing chamber and impacting the securely held specimen in the fixture. In this research, three parameters were used: slurry velocity (20 and 40 m s^{-1}), impact angles (30 and 90°), and sand concentrations (20,000 and 30,000 ppm). A fixed distance of 50 mm between the surface of the sample and the tip of the nozzle is maintained for all experiments. All the slurry erosion tests were carried out in compliance with ASTM G-73 standards. The specimen is placed in the holding fixture, and the angle range is varied from 15 to 90° at a step size of 15°, allowing the slurry to impact the specimen's surface by changing the various parameters. Silica sand collected from the riverbank contains particles with irregular shapes and sharp edges, which make it an effective erodent for slurry erosion tests. The particle sizes of 250 µm were sieved and mixed with tap water to prepare the slurry mixture for testing. The samples are washed with acetone to remove dirt, oil, and any attached matter from the sample surface before and following each slurry test, and the corresponding weight is measured using a weighing scale with a precision of 0.01 mg [Contech, CA224]. Each slurry test lasts 5 hours, with sample weight loss recorded at 30-minute intervals. Following weight measurement, calculate the volume loss of coatings by taking density into account.

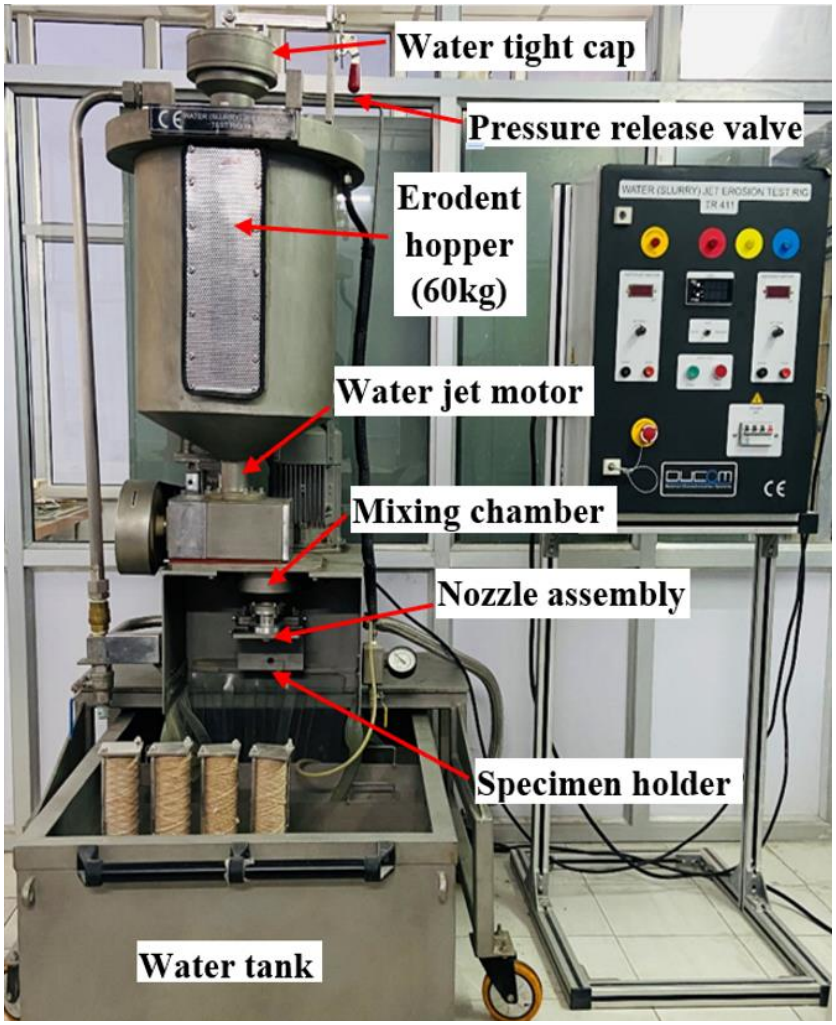

Figure 2. *Slurry jet erosion test rig setup [24]*

Electrochemical corrosion test

The potentiodynamic characteristics of two coatings were investigated using a three-electrode system with a potentiostat (Model 1010E, *Gamry Instruments)* at a scanning rate of 1 mV s^{-1}. The two WC-10Co-4Cr coated samples, each with an area of 1 cm^2, were immersed in a sodium chloride (NaCl) electrolyte. Using a standard three-electrode system, the corrosion parameters (E_{corr} and i_{corr}) of both coatings were measured. A saturated calomel electrode (SCE) functioned as the reference electrode, graphite operated as the counter electrode, and the coated sample treated as the working electrode in the standard electrochemical corrosion setup. The corrosion test setup employed a 3.5 wt.% NaCl solution as the working electrolyte. The electrochemical corrosion test is comprised of two main tests: open circuit potential (OCP) and potentiodynamic polarization test (PPT). The coated surface was dipped in a 3.5 wt.% NaCl solution at ambient temperature for an hour to allow for the establishment of a stable electrochemical condition. After the open circuit potential had stabilized, polarization curves were acquired at a scan rate of 1 millivolt per second (1 mV s^{-1}). Then, a plot of E versus Log I was constructed, and the meeting point of the anodic and cathodic polarization curves with their respective linear fits was identified and corresponding corrosion parameters (corrosion potential and corrosion current density) values were determined using the Tafel extrapolation method. To obtain an average value, at least four separate sets of experiments were performed on each specimen.

Results and discussion

Microstructure of substrate material

The microstructure of cast steel 21-4N steel and solution-treated steel is indicated in Figures 3(a) and 3(b). The heterogeneous structure of cast steel typically depicts two distinct phases, namely, the austenitic matrix phase (bright region) and carbide bunches (dark region), as shown in Figure 3(a). The cast steel microstructure contains two types of carbides, such as M_7C_3 and $M_{23}C_6$ (M can be Cr, C, and Fe) [25]. Since cast steel contains a high carbon content, it is generally chromium-sensitive, resulting in chromium carbide precipitation. These carbide precipitates were identified all along the grain boundary and within the austenite matrix [26]. The optical micrograph indicates that $M_{23}C_6$ carbides are located at grain boundaries, which is the most beneficial location. After obtaining sufficient energy from the heat treatment, chromium and carbon elements could move rapidly into the matrix, with grain boundaries being the beneficial location for carbide precipitation [27]. The optical microstructural image of solution-treated 21-4N steel (1150 °C for 120 min) is shown in Figure 3(b). This image (Fig. 3(b)) reveals that the volume fraction of carbides was significantly low, and a tiny fraction of carbides were concentrated at the grain boundary. Furthermore, solution treatment at an optimal temperature (1150 °C for 120 min) results in more uniform carbide dissolution in the austenitic matrix and a substantial number of twins appearing within the grain boundary region (complete carbide dissolution at the grain boundary). The reduction in carbides was attributed to the rapid penetration of chromium and carbon elements into the austenite matrix after obtaining the required energy from the heat treatment. Hence, the solution-treated (1150 °C for 120 min) 21-4N steel microstructure exhibits complete dissolution of carbide in the austenitic matrix, and a uniform austenitic phase was obtained as compared to the cast structure is depicted through optical micrographs.

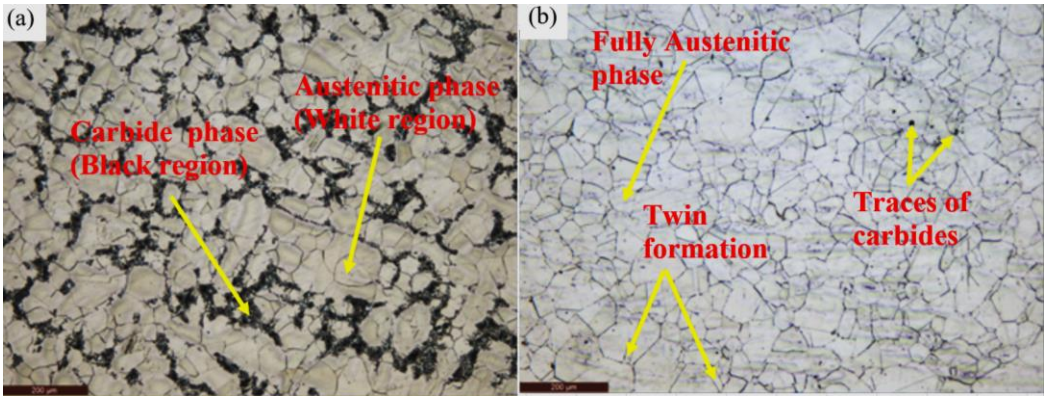

Figure 3. *Optical micro graphical microstructure of cast 21-4N steel (a) solution-treated 21-4N steel at 1150 °C and (b) 120 min*

Microstructure of coatings

Figure 4 indicates the cross-sectional microstructural photographs of two coatings obtained with FESEM and the EDS plot.

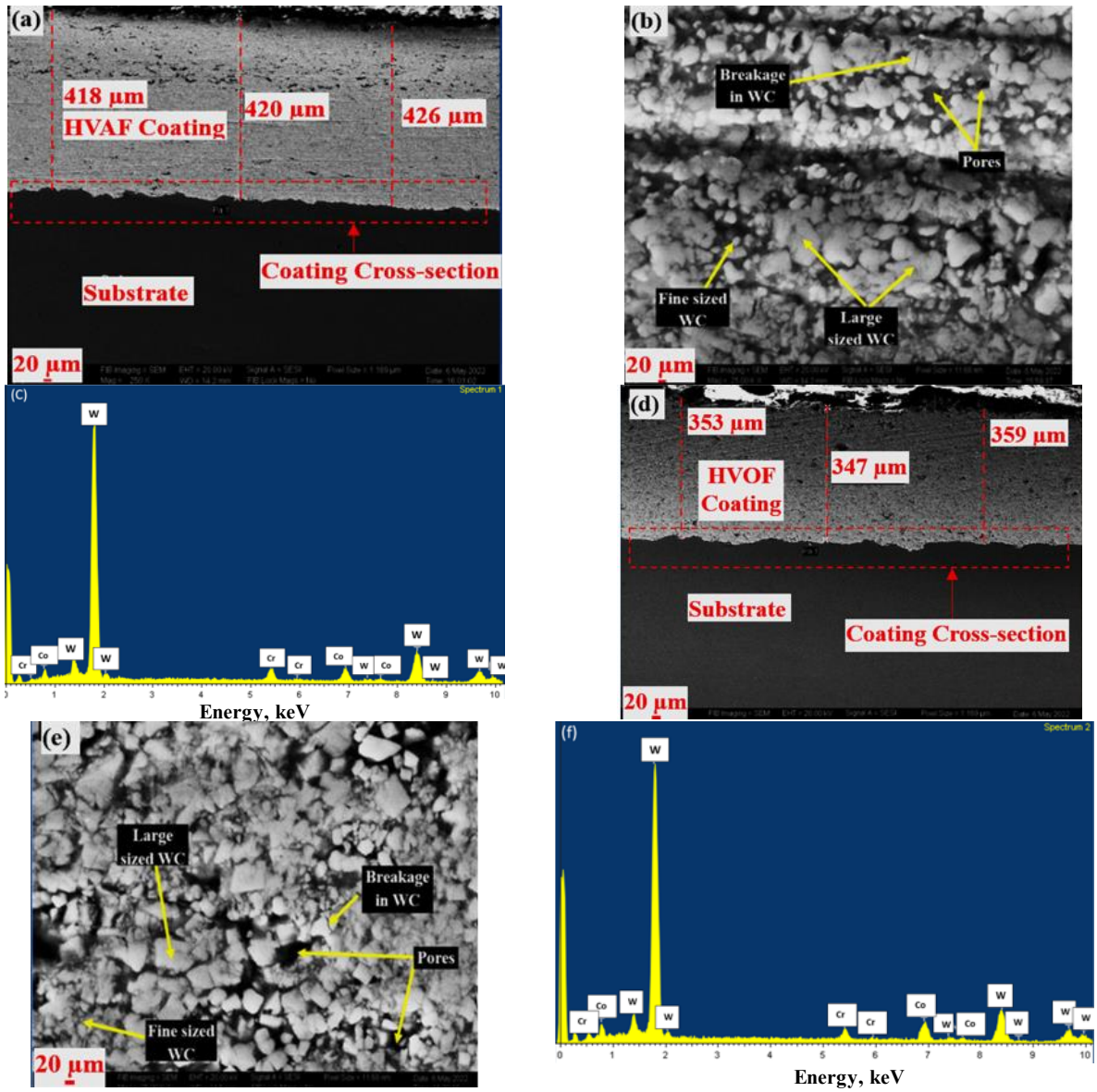

Figure 4. *Cross-sectional micrographs images of high and low magnification of (a and b) HVAF sprayed WC-CO-Cr coating, (d and e) HVOF sprayed WC-CO-Cr coating, EDS graph of (c) HVAF sprayed WC-Co-Cr coating, and (f) HVOF sprayed WC-Co-Cr coating*

The HVAF sprayed coating was observed to have an average thickness of around 421 µm, Figure 4(a) and the HVOF sprayed coating was observed to have an average coating thickness of around 353 µm, Figure 4(d). FESEM microstructure images present low and high-magnification views. Both coatings exhibit a robust and uniform structure in their micrographs, demonstrating strong bonding with the underlying substrate material. Further, each coating displays a certain level of laminar microstructure. In the HVOF coating, the presence of larger tungsten carbide (WC) particles within the binder matrix, and in certain areas, there are instances where WC particles appear to adhere to the coating with less surrounding binder material. Meanwhile, the HVAF coating displays a more consistent and uniform distribution of finer WC particles within the binder matrix [28]. Upon closer inspection of the high magnification images, Figures 4(b) and 4(e), some discernible pores and instances of WC particle breakages become apparent [29-31]. These breakages are attributed to the combination of high-velocity impact and the partially molten state of the particles impacted against the hard substrate material. It was also observed from images 4 (a) and 4 (d) that the pores that appear in the HVAF coating are fewer than in the HVOF coating. Furthermore, HVOF-fabricated coatings exhibit a non-uniform structure with more pores, while HVAF-sprayed coatings display a more compact structure with fewer pores. This distinction can be attributed to the intrinsic variations in the spraying processes. Specifically, the unique properties of the HVAF process contribute to the formation of a more tightly packed structure with reduced porosity.

Phase constitutions of coatings

Figure 5 shows XRD images of the original powder, HVAF, and HVOF deposited coatings. The graph of sprayed powder revealed that WC (JCPDF 00-51-0939) was the dominant phase, with a small amount of Co (JCPDF 15-806), W (JCPDF 00-004-0806), and Co_3W_3C (JCPDF 01-078-3750) phases being present. With WC as the dominant phase, minor phases of $Co_{12.9}Cr_{17.1}$ (JCPDF 01-080-8333) and W_2C (JCPDF 35-776) were detected in the HVAF coating. Furthermore, in the case of HVOF, the sprayed coating exhibits WC as a major phase with smaller traces of $Co_{12.9}Cr_{17.1}$, Co_3W_3C and W_2C (JCPDF 35-776) phases [32].

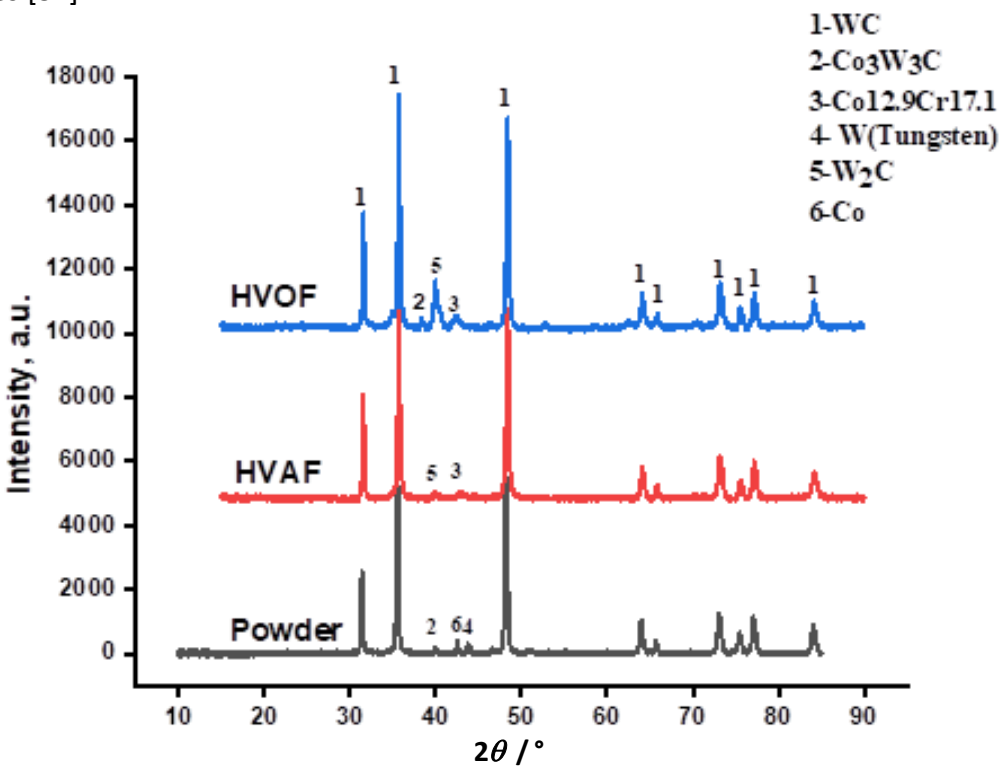

Figure 5. *Phase analysis (XRD) of powder, HVOF, and HVAF sprayed coating*

It is worth noting that the WC particles are transformed, including decarburization and dissolution, which lead to the formation of additional phases, including the presence of di-tungsten carbide (W_2C) in both coatings [33]. However, the diffraction peak of W_2C in the HVOF coating is higher than that of the HVAF coating. These results were consistent with previous work that used a similar powder as found in the literature [34-36]. Further, owing to the vaporization of a small amount of Co phase, no detectable cobalt-contained phases were present. However, both coatings demonstrate a noticeable quantity of Co-Cr-rich phase. *i.e.,* $Co_{12.9}Cr_{17.1}$ (42.638 degrees), as a similar phase is reported in the literature [37]. Hence, the High-Velocity Air Fuel (HVAF) process, by utilizing air instead of oxygen, can significantly impact the characteristics of the sprayed coating, particularly in reducing the effect of decarburization and minimizing the brittleness of the coating [38-39].

Microhardness analysis

The microhardness of the samples was assessed at five different locations, and the average was computed. This approach is necessary because the microhardness value can vary depending on the composition of the material. When the indentation occurs in areas with harder phases, the microhardness tends to be higher. Conversely, when the indent is located in regions with softer phases or defects, the microhardness may be lower. The average microhardness readings for the uncoated specimen were observed to be 164 HV, while for the HVAF-coated specimen, it was 1582 HV, and for the HVOF specimen, it was 1398 HV. The probable reason for variations in microhardness values between the specimens could be attributed to differences in material composition, grain structure, presence of defects, or variations in coating thickness. For instance, the HVAF-coated specimen might exhibit higher microhardness due to the application of a hard coating layer, while the uncoated specimen may have a lower microhardness value due to the absence of such coatings. Similarly, the HVOF specimen might have intermediate microhardness values depending on the specifics of the coating process and material used. Further, the indent micrographs of coated, HVAF, and HVOF sprayed samples are presented in Figure 6.

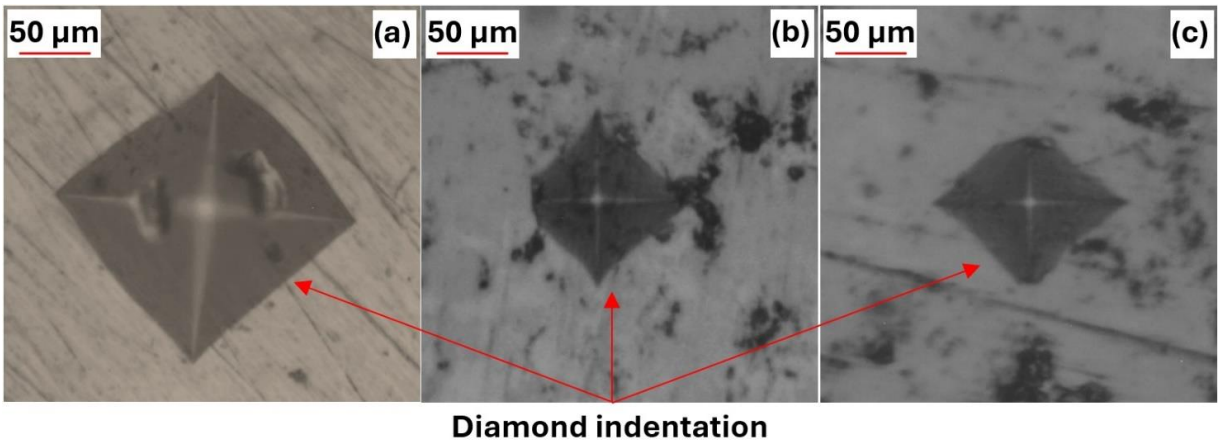

Figure 6. *Indent micrographs for (a) uncoated sample, (b) HVAF sprayed sample, and (c) HVOF sprayed sample.*

Fracture toughness, roughness, and porosity of coatings

The HVAF coatings showed a lower surface roughness of 2.16±0.12 µm against the HVOF coating roughness of 4.68±0.45 µm, which may be due to the use of fine powder particles in the HVAF process. In addition, the fracture toughness of HVAF coating (5.69±0.24 MPa $m^{1/2}$) is higher than that of HVOF coating (4.29±0.35 MPa $m^{1/2}$), possibly due to less porosity, improved bonding between WC particles, and the binder matrix offering higher resistance to cracking. The HVAF-

sprayed coating has a lower measured porosity (0.97±0.13 %) than the HVOF-sprayed coating (1.26±0.14 %), indicating that it is slightly more compact and has fewer pores. The microstructure analysis of two as-sprayed coatings was determined from SEM micrographs (20,000× magnification) of the coating cross-section using Magni-scientific image analysis software (Divergent Rays Computing Inc.). The porosity volume fraction (%), carbide volume fraction (%), carbide size (µm), binder volume fraction (%), and density (g cm^{-3} values are listed in Table 2.

Table 2. *Porosity volume fraction, carbide volume fraction, binder volume fraction, and density (gm cm^{-2}) of HVAF and HVOF sprayed coatings*

	HVOF	HVAF
Porosity volume fraction, %	1.26±0.14	0.97±0.13
Carbides volume fraction, vol.%	63.3±1.5	76.9±1.2
Carbides size, µm	1.1± 0.5	1.21± 0.3
Binder volume fraction, vol.%	35.05±0.63	22.01±0.31
Density, gm cm^{-3}	12.64	13.60

Slurry erosion responses of developed coatings

The cumulative volume loss from slurry erosion experiments can be influenced by different parameters, namely slurry velocity, impact angle, and sand concentration parameters. Goyal *et al.* [40] proposed a correlation for the wear rate of hydro turbine materials, Equation (1).

$$E_W = k\, V^p\, d^q\, C^r \quad (1)$$

where E_W represents slurry rate, V denotes the speed at which slurry impinges on the sample surface, d specifies the average erodent size, and C denotes sand concentration in the slurry. Values of k, p, q, and r denote the corresponding exponents of slurry velocity, average erodent size, and sand concentration. In the current research work, slurry erosion experiments were conducted to evaluate the performance of the HVOF and HVAF coatings under varying slurry velocity, impact angle, and sand concentration conditions at 2 levels. The parametric variation at 2 levels was chosen to maintain experimental tractability while capturing meaningful trends in slurry erosion behavior. By limiting the levels of variation, the focus on investigating the most significant factors influencing erosion resistance without introducing unnecessary complexity can be done. Furthermore, the selected levels for each parameter were based on previous literature findings and practical considerations. For example, the slurry velocity was varied at 20 and 40 m s^{-1} to encompass a range commonly encountered in industrial applications, allowing for a comprehensive assessment of erosion resistance under typical operating conditions [1]. Similarly, impact angles of 30 and 90° were chosen to represent both acute and normal impingement angles, reflecting real-world scenarios where hydroturbine components are subjected to varying degrees of erosion wear [1]. Lastly, sand concentrations of 20,000 and 30,000 ppm were selected to cover a range of abrasive particle densities typically encountered in slurry environments.

Effect of slurry velocity

The slurry velocity of impinging sand particles had a significant effect on the volume loss of both coatings. When particles in a slurry possess higher kinetic energy, they strike the material surface with more impact force. It has been revealed from the literature that more forceful impacts on the target material led to greater or higher volume loss at higher slurry velocity. Figure 7 bar chart illustrates the impact of varying slurry velocity (20 and 40 m s^{-1}) on two sprayed coatings at a sand concentration of 20,000 ppm with a 90° impact angle. We observed that the volume loss of both coatings is higher for

a normal impact angle (90°). This fact was confirmed by various researchers in their reported work [7-9,39]. Islam *et al.* [41] found that at lower velocities, the kinetic energy of the sand particles may not be sufficient to cause significant material removal. Instead, impacts are primarily elastic, meaning they don't exceed the threshold energy required for material removal. On the other hand, if the sand particles acquire more kinetic energy as a result of their increased velocity, it consequently leads to more material removal. According to Maekai *et al.* [42], impinging sand particles must have the same or higher than the critical energy to remove material from the substrate surface. As expected, sand particles achieve more critical energy at higher slurry velocities, resulting in higher material removal in comparison to lower velocities. As reported by Ramesh *et al.* [43], it corroborates the understanding that increasing slurry velocity directly translates to higher kinetic energy of the sand particles, leading to more focused and forceful impacts at multiple locations on the target material surface. This analysis demonstrates a significant difference in volume loss between the HVAF-sprayed coating and the HVOF-sprayed coating under two slurry velocities. At 20 m s^{-1} slurry velocity, the HVAF coating experienced 1.39 times lower volume loss as compared to the HVOF coating. Further, at 40 m s^{-1} slurry velocity, the HVAF coating demonstrated a lower volume loss, with a factor of 1.76 times as compared to the corresponding HVOF coating [44]. Hence, HVAF-coated steel showed a higher erosion resistance than HVOF coating at all velocities under given conditions. Therefore, the HVAF coating has the highest erosion resistance due to its high hardness, less porosity, and higher fracture toughness than the HVOF coating.

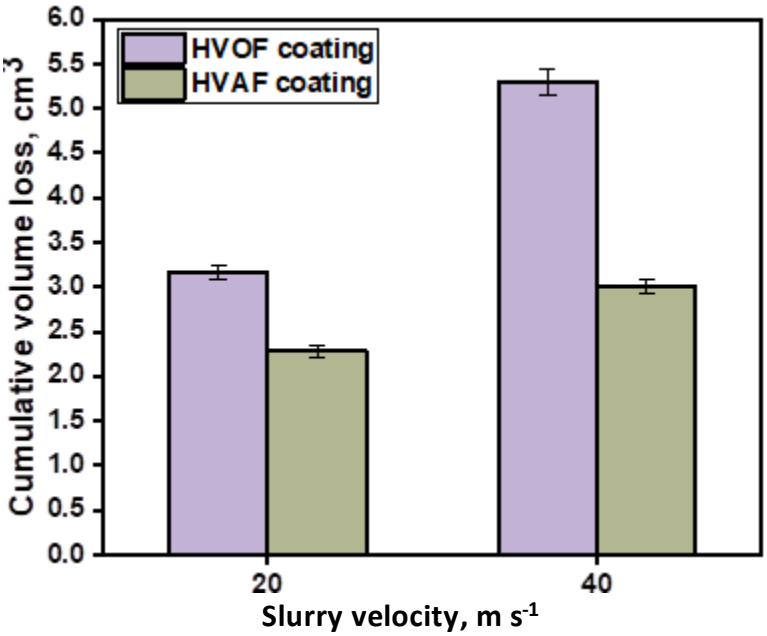

Figure 7. *Erosion volume loss of coatings (HVOF/HVAF) at different slurry velocities.*

Effect of impact angle

Hydro turbine parts in hydroelectric plants are prone to erosion wear during service due to the action of a wide range of impact angles at various locations. The erosion of target material at different angles can identify the angles that pose the highest risk of erosion under specified test conditions. These investigations aid in understanding the kind of erosion (whether it is ductile or brittle) under specific conditions. According to the literature review, ductile materials tend to exhibit more pronounced erosion at sharp angles, typically falling within the range of 15 to 30°, but at the higher angle of impact (90°), the erosion rate gradually decreases. For brittle materials, erosion wear tends to be less severe at low impingement angles. However, an increase in impact angle causes the force

of the impinging particles to cause substantial damage to the target material. As a result, brittle materials resist erosion wear at acute angles but are more vulnerable to shear stress and deteriorate more rapidly at normal angles [45]. Figure 8 bar chart illustrates the impact of varying impact angles (30 and 90°) on two sprayed coatings at a sand concentration of 30,000 ppm with 40 m s^{-1} slurry velocity. It appears from the figure that a trend in slurry erosion volume loss for both HVAF and HVOF-coated steel changes with increases in impact angles. This is the fragile nature of the coatings as reported by researchers [46]. Malik *et al.* [47] noticed that materials with high hardness, such as ceramics and cermets, withstand erosion at lower angles. In contrast, ductile metals suffer more material loss due to higher shear forces. In contrast, ductile material absorbs a significant amount of impact energy at normal angles, resulting in reduced material loss. In comparison, HVAF-coated steel showed higher erosion resistance than HVOF coating at all impact angles under given conditions. At a 30° impact angle, the HVAF coating experienced 1.53 times lower volume loss compared to the HVOF coating. In contrast, at a 90° impact angle, the HVAF coating demonstrated a lower volume loss, with a factor of 1.84 times as compared to the corresponding HVOF coating. However, the erosion mechanism changed from plowing to plastic deformation as the angle changed from 30 to 90°. This aligns with the fundamental principles of slurry erosion, where the angle at which particles impinge on a surface can significantly influence the volume loss of both coatings.

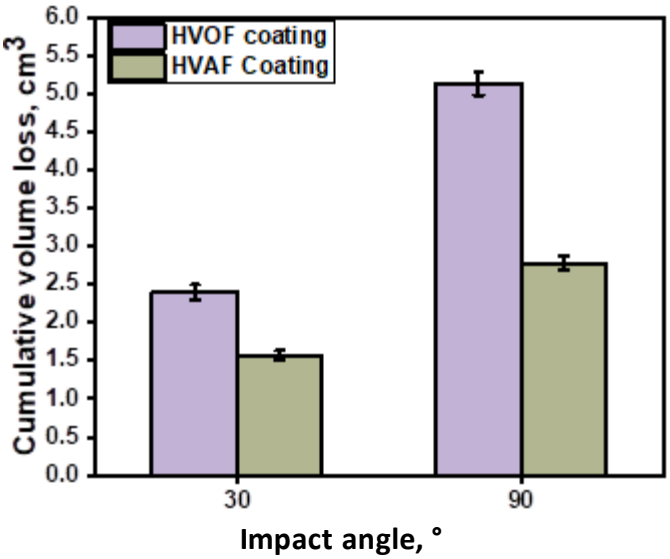

Figure 8. *Erosion volume loss of coatings (HVOF/HVAF) at different impact angles.*

Effect of sand concentrations

The concentration of sand particles in the slurry can have a significant effect on the erosive wear of the target material. At lower concentrations of sand particles in the slurry, there are fewer abrasive particles available for impact with the target surface. Consequently, the erosive effects are less pronounced. However, as the concentration of sand particles increases, more particles are available to interact with the target surface. This leads to a higher frequency of impacts and abrasions, resulting in an increased loss of material from the surface of the target. Figure 9 bar chart illustrates the impact of varying sand concentrations (20,000 and 30,000 ppm) on two sprayed coatings at a slurry velocity of 20 m s^{-1} with a 30° impact angle. The variation in volume loss with sand concentration for both coatings is an important finding. According to these studies [8,9,22,48-49], an increase in sand concentration would increase the frequency of indentation, resulting in more surface damage and material loss. Du *et al.* [50] express a similar view that an increase in sand concentration promotes more sand particles striking the target surface per unit time, causing more

mass loss. However, some researchers [51] reported that higher sand concentrations contributed to a reduction in mass loss. It is supported by the fact that at higher sand concentrations, inter-particle collision, the interaction between rebounding particles with the fresh incoming particles causes a shielding effect, which reduces kinetic energy, thereby altering the penetrating path of the sand particles, causing them to strike at different angles or bypass the impact surface, resulting in a lower weight loss. As reported by Kleis *et al.* [52], collisions among particles, particle motion, and sedimentation could enhance the effect of sand concentration on slurry erosion wear. At 20,000 ppm, the HVAF coating experienced 1.33 times lower volume loss compared to the HVOF coating. In contrast, at a 90° impact angle, the HVAF coating demonstrated a lower volume loss, with a factor of 1.53 times as compared to the corresponding HVOF coating. Hence, HVAF-coated steel showed the highest erosion resistance to HVOF coating at all sand concentrations, owing to improved hardness, lesser porosity, and higher fracture toughness than HVOF coating.

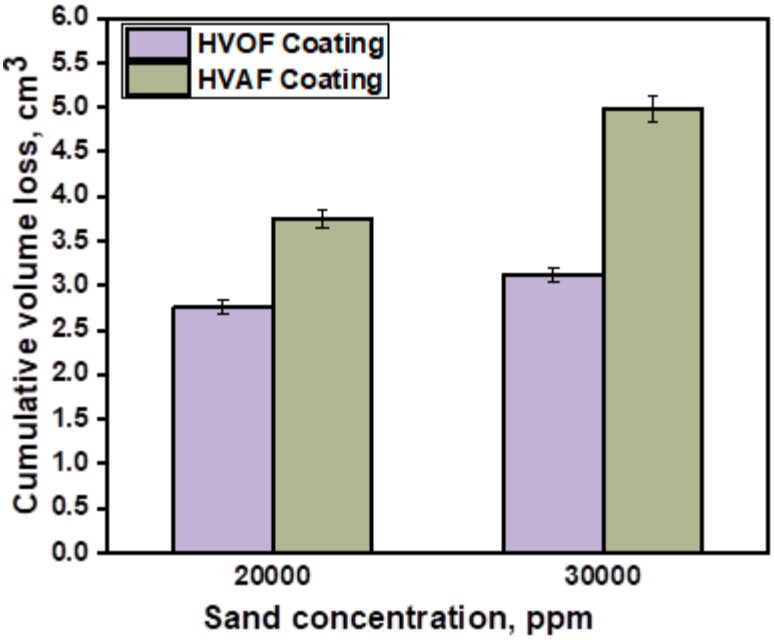

Figure 9. *Erosion volume loss of coatings (HVOF/HVAF) at different sand concentrations.*

Analysis of wear specimens

The impact of high-velocity sand particles causes the gradual degradation of coating material during service. To understand the mechanisms behind the removal of coating material are investigated by performing a surface morphological analysis of eroded samples under different conditions using SEM.

Effect of slurry velocity

Figure 10 indicates SEM images of eroded surfaces of HVOF/HVAF fabricated coatings by the effect of distinct slurry velocities (20 and 40 m s^{-1}) at a normal impact angle. The volume loss of both coatings is observed to increase with increasing slurry velocity. This is attributed to the increase in impact energy of sand particles on the surface of coatings, which leads to more forceful impacts, which subsequently result in greater mass loss from the coatings. Both coatings depict more volume loss at higher slurry velocities (40 m/s), but HVAF sprayed coating has lower volume loss as compared with HVOF sprayed coating at all slurry velocities, keeping other conditions identical. The SEM images of HVOF/HVAF coatings eroded at lower slurry velocity (20 m s^{-1}) are shown in Figures 10(a) and 10(b). The typical erosion mechanisms of the coatings were found to be craters, lip-based

plastic deformation, and spalling. The impact of sharp-edged sand particles created some deep craters in the HVOF coatings, as shown in Figure 10(a). The growth of smaller cracks and the removal of WC particles caused by crack coalescence in the inter-splat result in coating spalling in the form of debris. In comparison, HVAF coatings display a smoother surface than HVOF sprayed coating (Figure 10(b)). Figures 10(c) and 10(d) show the eroded images of HVOF/HVAF coatings at 40 m s^{-1} slurry velocity. At this velocity, coatings show enhanced damage compared to lower velocity (20 m s^{-1}), which increases the network of cracks and results in coating spallation, leading to more mass loss. It has been noticed that increasing slurry velocity causes more spalling of coatings due to WC grain detachment and more visible craters. Similar observations were made by the researcher in their work [53-55]. However, increasing the slurry velocity may not have an impact on the change in the mechanism of coating material removal in the current study. Thus, the combination of high hardness, fracture toughness, low porosity, and a dense structure helps to maximize the resistance of HVAF coatings.

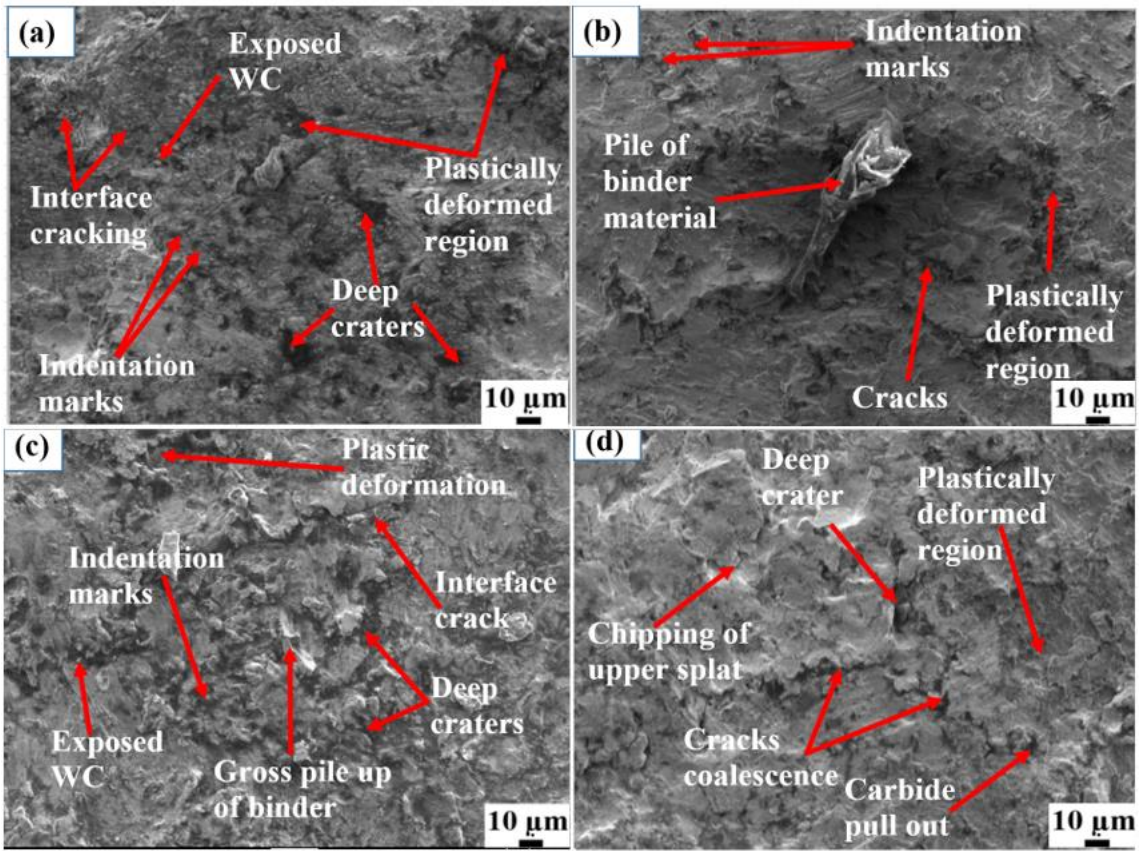

Figure 10. *Eroded SEM images of coatings at jet velocity of 20 m s^{-1} for (a) HVOF sprayed coating, (b) HVAF sprayed coating, and at 40 m s^{-1} for (c) HVOF sprayed coating, (d) HVAF sprayed coating*

Effect of impact angle

Figure 11 illustrates SEM images of eroded areas of both WC-CO-Cr coatings subjected to different impact angles (30 and 90°). The HVOF process typically depicts the coatings with larger tungsten carbide (WC) particles as observed from the microstructure. These larger particles may have more interstitial spaces between them, resulting in a higher porosity than HVAF coatings. Due to the larger particle size and potentially higher porosity, the erosive action of sand particles can more easily disengage or fracture individual WC particles from the binder matrix. This further diminishes the overall erosion resistance of the coating. As the impact angle increases, the energy transferred to the coating surface during the erosive process also increases, resulting in greater

material removal and higher volume loss. Both coatings exhibit the highest amount of volume loss at higher impact angles (90°), but HVAF sprayed coating has better resistance to erosion than HVOF sprayed coating at all impact angles, keeping other conditions identical. This behavior ideally represents the brittle nature of the fabricated coatings. Figures 11(a) and 11(b) SEM images provide valuable insight into the erosive mechanisms and wear patterns observed in HVOF and HVAF sprayed coatings subjected to an acute angle of 30°. It reveals ploughing marks caused by the tangential action of sand particles, binder matrix removal, micro-cutting, and deep grooves responsible for coating material loss. The sand particles slide against the coating, eradicating the softer binder material (Co/Cr) from the coating surface, leaving WC particles exposed to the coating surface. Then, further impingement of sand parties causes them to fall by leaving shallow craters. Figures 11(c) and 11(d) reveal the surface morphology of damaged surfaces of coatings at normal impact angles (90°). The coating spalling occurs mainly by plastic deformation, resulting in the ejecting of coating material. It was observed that owing to the effect of fatigue stress induced by the sand particles on the impact area of the coating, cracks could develop at the stress concentration areas. Further, cracks coalesced, resulting in the spalling of coatings and enhancing the mass loss of coating material. These findings align with the work of Liu *et al.* [56]. Hence, coatings spallation by fatigue stress of sand particles was the main mechanism of loss of coating material at a normal impact angle. HVAF-sprayed coatings had less surface damage than HVOF-sprayed coatings. Thus, the combination of high hardness, fracture toughness, low porosity, and a dense structure helps to maximize the resistance of HVAF coatings.

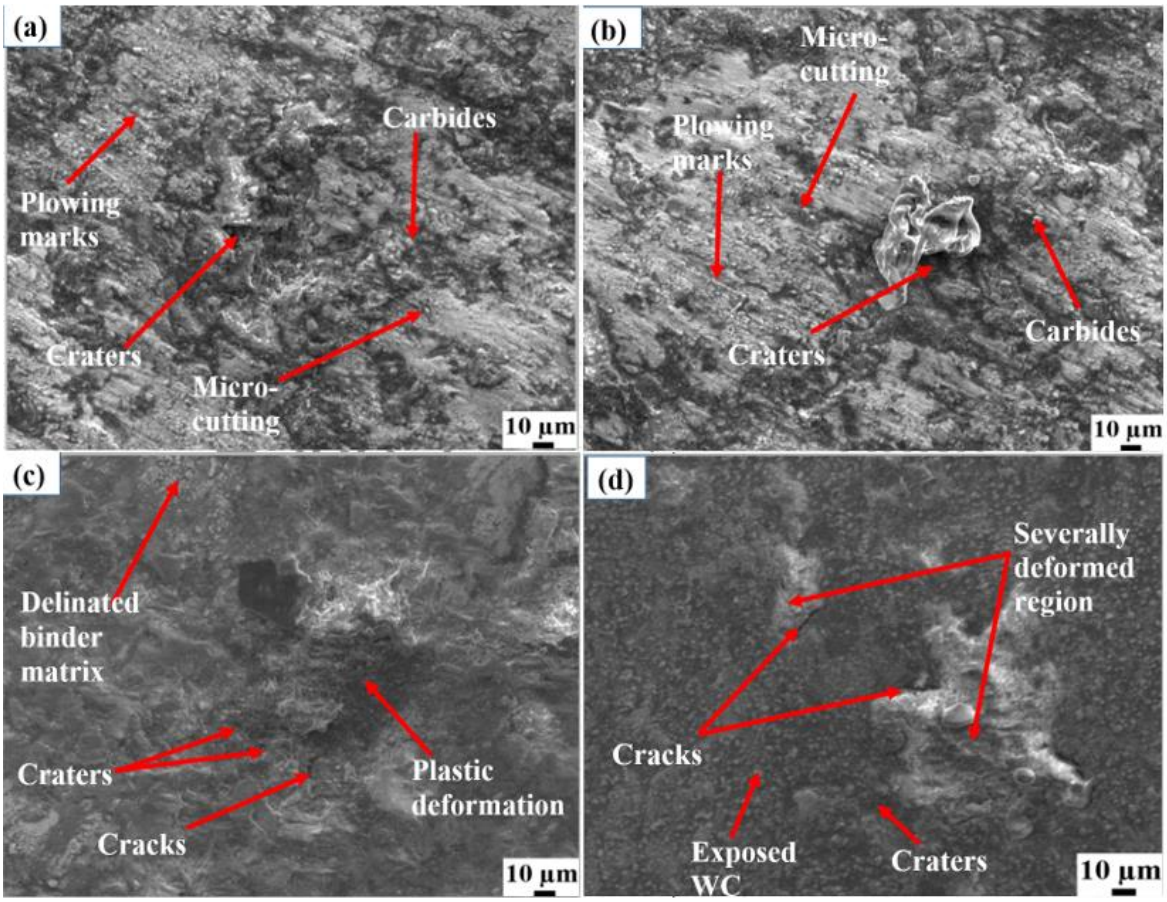

Figure 11. *Eroded SEM images of coatings at 30° impact angle for (a) HVOF sprayed coating, (b) HVAF sprayed coating, and at 90° for (c) HVOF sprayed coating, (d) HVAF sprayed coating*

Effect of sand concentrations

Figure 12 illustrates SEM images of eroded areas of both WC-CO-Cr coatings subjected to different sand concentrations (20,000 and 30,000 ppm). The volume loss of both coatings is observed to increase with increasing sand concentrations. For all concentrations, HVAF coatings perform better than HVOF coatings in terms of erosion resistance. As sand concentration goes up from 20,000 to 30,000 ppm, subsequently coatings damage elevates. The HVAF sprayed coating displays a smoother surface than the HVOF-coated surface for all sand concentrations. The main mechanism of material is the plowing of coating material, which leads to the formation of lips. From Figures 12(a) and 12(b), coatings are removed by plowing action followed by cutting off material from the impacted area, leading to the formation of smaller craters and carbides being exposed to the surface. Figures 12 (c) and 12(d) show that smaller craters were formed due to WC being pulled out from the binder material. Similar observations were made by [57] in their investigation. Thus, the improved properties of HVAF coatings help maximize the resistance compared to HVOF coatings.

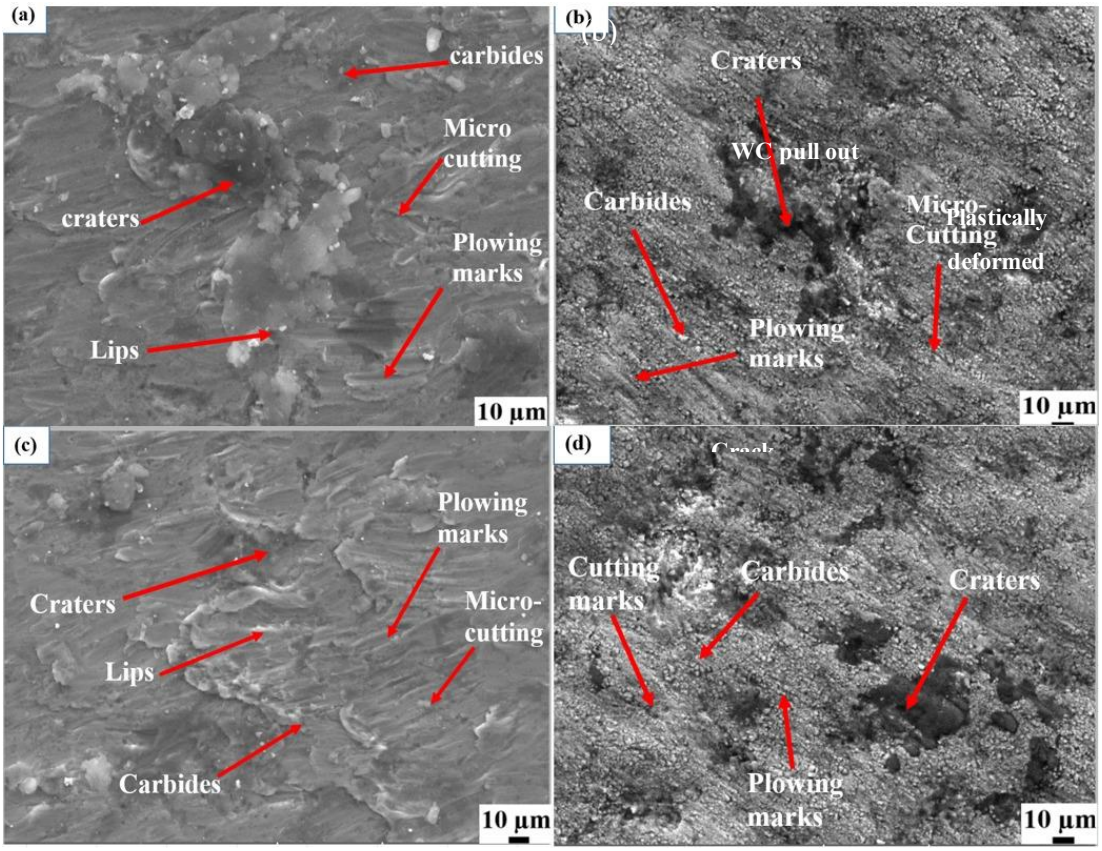

Figure 12. *Eroded SEM images of coatings at 20000 ppm slurry concentration for (a) HVOF sprayed coating, (b) HVAF sprayed coating, and at 30000 ppm for (c) HVOF sprayed coating, (d) HVAF sprayed coating*

Electrochemical corrosion test

The polarization curves (refer to Figure 13) obtained from this technique can provide important information about the corrosion resistance of coatings (HVOF/HVAF). The coated specimen was soaked in a 3.5 wt.% NaCl solution for 1 hour for stabilization of the OCP. After the establishment of a consistent OCP through preconditioning, polarization curves were obtained. These electrochemical parameters, such as the corrosion potential (E_{corr}) and current density (I_{corr}) can be determined from the polarization curves using the Tafel extrapolation method. This method involves fitting linear segments to both the anodic (corrosion) and cathodic (protection) portions of the polarization curves. These linear fits are used to estimate the corrosion potential (E_{corr}) and corrosion current

density (i_{corr}) by identifying the intersection point of the two lines. These values of Ecorr and i_{corr} for the two coatings are provided in Table 3. Specifically, the HVAF-sprayed coating exhibits an Ecorr value of -0.392 V, while the HVOF coating registers an E_{corr} value of -0.331 V. The i_{corr} value for the HVAF coating is measured at 15 A cm^2, indicating a lower rate of corrosion compared to the HVOF coating, which records an i_{corr} value of 40 A cm^2. This suggests that the HVAF-sprayed coating exhibits superior corrosion resistance under the given conditions. These findings were aligned with previous research [6,31] specifically confirming that the HVAF-fabricated WC-10Co-4Cr coating displays outstanding corrosion resistance. This is often attributed to factors such as the presence of crystalline Cr phase, lower porosity, and a homogeneous microstructure devoid of visible microcracks (as observed in Figure 4 and Table 2). It is acknowledged that corrosion typically initiates in flawed coating regions, including interconnected microcracks and pores prevalent in highly porous coatings. Additionally, various studies [53-54] have reported that chromium (Cr), a principal coating constituent, can generate a passive layer rich in chromium. This layer plays a pivotal role in preventing the dissolution of the binder matrix in sodium chloride solutions. The amalgamation of these factors underscores the enhanced corrosion resistance observed in the HVAF-fabricated WC-10Co-4Cr coating compared to its HVOF-sprayed counterpart.

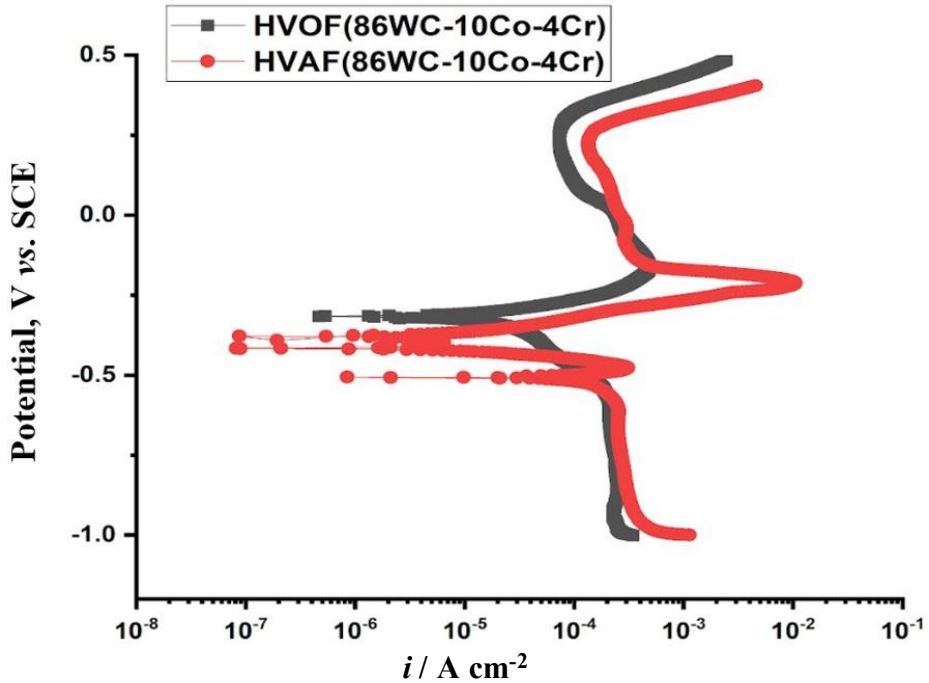

Figure 13. *Polarization curves of the HVOF/HVAF fabricated coatings in a 3.5 wt.% NaCl solution*

Table 3. *Corrosion potential and current density values of HVOF/HVAF fabricated coatings*

Coatings	*E* / V	i_{corr} / µA cm^{-2}
HVOF (86WC-10Co-4Cr)	-0.331	40
HVAF (86WC-10Co-4Cr)	-0.392	15

Analysis of corrosion specimen

Figure 14 depicts the corrosion surface morphology of HVOF/HVAF-developed WC-10Co-4Cr coatings. A significant number of WC particles were observed on the corrosion surfaces, resulting from binder material melting around the point of contact between WC particles and the binder matrix. Furthermore, the dissolution of a selective area of the binder matrix in a NaCl solution leads to WC particle dislodgement and microcavity formation [58]. The corrosion morphology depicted in

Figures 14(a) and 14(b), provides critical insights into how the HVOF/HVAF coatings respond to corrosive environments. The examination of the corrosion morphology revealed the presence of several distinctive features such as microcavities, corrosion pits, and micro-cracks as a result of the fallout of WC particles owing to binder material dissolving into NaCl. On the other hand, HVAF coating exhibits fewer microcavities, and microcracks due to reduced porosity are significant. Concurrently, an extremely thin white film forms on the surface of both coatings, caused by the presence of the Cr component in the coating material, which could produce a passive film, preventing corrosion through Cr element passivation. Other researchers observed similar phenomena in their study [59-61], particularly the formation of chromium oxide as a passive protective film on the surface of the coating, thereby suppressing the dissolution of binder material, resulting in less fall off of WC particles from the coating surface and improved corrosion resistance. According to the previous study [6,31,62], these facts may have considerable effects on the corrosion resistance of the WC-Co-Cr coating in several ways. The micro-galvanic corrosion mechanism is common in composite materials, especially those with dissimilar phases or constituents. While the WC particles are cathodically protected, the binder matrix is exposed to anodic corrosion. The oxidation of the matrix material releases metal ions into the electrolyte, resulting in the corrosion of the binder matrix. However, in comparison to coatings, the substrate material 21-4N steel has a lower corrosion potential value. When NaCl electrolyte penetrates the coating/substrate interface through micro-cracks and pores, micro galvanic corrosion could occur. Therefore, binder material subsequently dissolves around the WC particle/binder matrix interface, causing WC particles to fall out of the coating by creating corrosion cavities or pits in the coating.

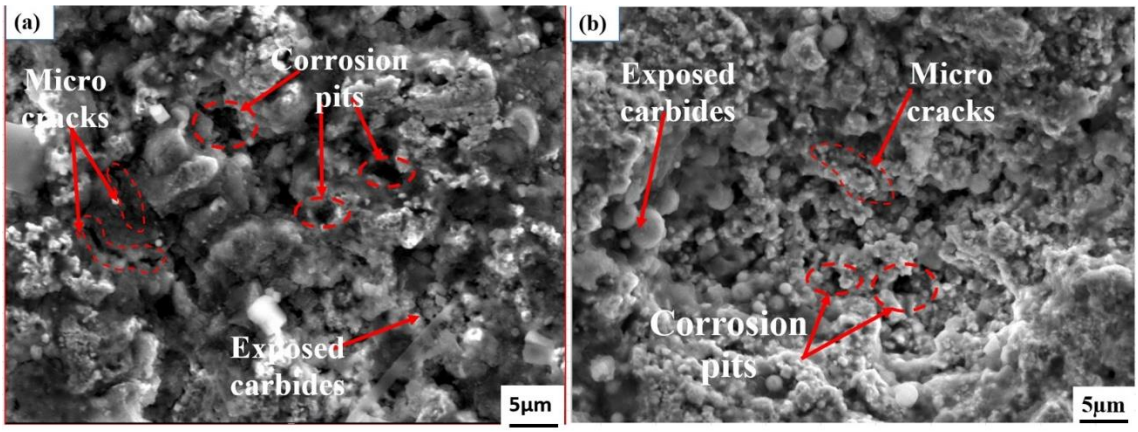

Figure 14. *Surface morphology of corroded WC-10Co-4Cr coatings: (a) HVOF and (b) HVAF*

Conclusions

1. The HVOF/HVAF fabricated WC-10Co-4Cr coatings had an appealing microstructure, and the HVAF sprayed WC-Co-Cr coating exhibited higher hardness (1582 HV), greater fracture toughness (5.69 MPa $m^{1/2}$), less decarburization, and lower porosity (0.97 %) as compared to HVOF sprayed coating.
2. The HVAF process, compared to HVOF, appears to be more effective in mitigating decarburization in the WC-10Co-4Cr coatings. This could be attributed to factors like lower combustion temperatures or the specific heating and cooling profiles associated with HVAF.
3. HVAF and HVOF fabricated coatings have demonstrated impressive performance in resisting slurry erosion and corrosion due to their high hardness and low porosity characteristics.

4. The synergistic combination of properties, which includes high hardness, fracture toughness, low porosity, a higher rate of carbide retention, and a dense structure, aids in improving the slurry erosion resistance of HVAF coatings over HVOF coatings.
5. The HVAF coating demonstrated outstanding corrosion resistance with respect to the HVOF coating, which can be attributed to its lesser porosity, consistent and bulky microstructure, and minimal cracks.
6. The damaged surface of the two coatings resulting from slurry erosion tests discloses the signs of plastic deformation, crater, gross removal of binder material, material removal by cracks coalescence in the binder matrix, and WC grain pull out owing to spalling.
7. The corrosion surface of the two coatings reveals that the binder material is susceptible to dissolution at the interface between the WC particles and the Co-Cr matrix, microcracks and corrosion pits were formed as a result of the WC particles being wiped out.

References

[1] V. Singh, A. Kumar Singla, A. Bansal, Impact of HVOF sprayed Vanadium Carbide (VC) based novel coatings on slurry erosion behaviour of hydro-machinery SS316 steel, *Tribology International* **176** (2022) 107874. https://doi.org/10.1016/j.triboint.2022.107874.

[2] V. Singh, A. Bansal, A. Kumar Singla, Response surface methodology (RSM) based analysis on slurry erosion behavior of laser textured and PTFE sprayed VC+ TiC coating deposited via HVOF, *Materials Today Communications* **36** (2023) 106843. https://doi.org/10.1016/j.mtcomm.2023.106843.

[3] V. R. Kiragi, A. Patnaik, T. Singh, G. Fekete, Parametric optimization of erosive wear response of TiAlN-coated aluminum alloy using Taguchi method, *Journal of Materials Engineering and Performance* **28** (2019) 838-851. https://doi.org/10.1007/s11665-018-3816-6.

[4] R. Kumar, K. Goyal, D. Bhandari, Slurry Erosion Behavior of Thermally Sprayed Nano YSZ Reinforced WC-10Co-4Cr Ceramic Nanocomposite Coatings, *Tribology Transactions* **66** (2023) 47-58. https://doi.org/10.1080/10402004.2022.2137446.

[5] M. Magdy EI-Rayes, M. Sherif EI-Sherif, S. Abdo Abdo, Comparative Study into Microstructural and Mechanical Characterization of HVOF-WC-Based Coatings. Crystals12 (2022) 969. https://doi.org/10.3390/cryst12070969.

[6] Y. Liu, W. Liu, Y. Ma, S. Meng, C. Liu, L. Long, S. Tang, A comparative study on wear and corrosion behaviour of HVOF-and HVAF-sprayed WC–10Co–4Cr coatings, *Surface Engineering* **33** (2007) 63-71. https://doi:10.1080/02670844.2016.1218194.

[7] H. Singh Grewal, S. Bhandari, H. Singh, Parametric study of slurry-erosion of hydro turbine steels with and without detonation gun spray coatings using Taguchi technique, *Metallurgical and Materials Transactions A* **43** (2007) 3387-3401. https://doi.org/10.1007/s11661-012-1148-y.

[8] D. Kumar Goyal, H. Singh, H. Kumar, V. Sahni, Slurry erosion behaviour of HVOF sprayed WC–10Co–4Cr and Al2O3+ 13TiO2 coatings on turbine steel, Wear **289** (2012) 46-57. https://doi.org/10.1016/j.wear.2012.04.016.

[9] G. Singh, S. Kumar, S. Satbir Sehgal, Erosion tribo performance of HVOF deposited WC-10Co-4Cr and WC-10Co-4Cr+ 2% Y2O3 micron layers on pump impeller steel, *Particulate Science and Technology* **38** (2018) 34-44. https://doi.org/10.1080/02726351.2018.1501780.

[10] G. Bolelli, L. M. Berger, T. Börner, H. Koivuluoto, L. Lusvarghi, C. Lyphout, P. Vuoristo, Tribology of HVOF-and HVAF-sprayed WC–10Co4Cr hard metal coatings: A comparative assessment, *Surface and Coatings Technology* **265** (2015) 125-144. https://doi:10.1016/j.surfcoat.2015.01.048.

[11] V. Kumar, V. Singh, R. Verma, A. Bansal, G. Ghosh, Cavitation-corrosion analysis of HVOF-sprayed WC-Co-Cr-graphene nanoplatelets coatings with LST pre-treatment. *International Journal of Refractory Metals and Hard Materials* **120** (2024) 106610. https://doi.org/10.1016/j.ijrmhm.2024.106610.

[12] K. Torkashvand, S. Joshi, V. Testa, F. Ghisoni, S. Morelli, G. Bolelli, L. Lusvarghi, F. Marra, M. Gupta, Tribological behavior of HVAF-sprayed WC-based coatings with alternative binders, *Surface and Coatings Technology* **436** (2022) 128296. https://doi.org/10.1016/j.surfcoat.2022.128296.

[13] S. L. Liu, X. P. Zheng, G. Q. Geng, Influence of nano-WC–12Co powder addition in WC–10Co–4Cr AC-HVAF sprayed coatings on wear and erosion behaviour, *Wear* **269** (2010) 362-367. https://doi.org/10.1016/j.wear.2010.04.019.

[14] Q. Wang, S. Zhang, Y. Cheng, J. Xiang, X. Zhao, G. Yang, Wear and corrosion performance of WC-10Co4Cr coatings deposited by different HVOF and HVAF spraying processes, *Surface and Coatings Technology* **218** (2013) 127-136. https://doi.org/10.1016/j.surfcoat.2012.12.041.

[15] Q. Wang, Z. Tang, L. Cha, Cavitation and sand slurry erosion resistances of WC-10Co-4Cr coatings, *Journal of Materials Engineering and Performance* **24** (2015) 2435-2443. https://doi.org/10.1007/s11665-015-1496-z.

[16] R. K. Kumar, M. Kamaraj, S. Seetharamu, A pragmatic approach and quantitative assessment of silt erosion characteristics of HVOF and HVAF processed WC-CoCr coatings and 16Cr5Ni steel for hydro turbine applications, *Materials & Design* **132** (2017) 79-95. https://doi.org/10.1016/j.matdes.2017.06.046.

[17] Y. Li, Y. Lian, J. Cao, L. Li, Solid particle erosion behavior of HVOF/HVAF sprayed WC-Co-Cr coatings, *Proceedings of the Institution of Mechanical Engineers, Part J: Journal of Engineering Tribology* **230/6** (2016): 634-643. https://doi.org/10.1177/1350650115608209.

[18] S. Hong, Y. Wu, Y. Zheng, B. Wang, W. Gao, G. Li, G. Ying, J. Lin, Effect of spray parameters on the corrosion behavior of HVOF sprayed WC-Co-Cr coatings, *Journal of materials engineering and performance* **23** (2014)1434-1439. https://doi.org/10.1007/s11665-014-0865-3

[19] A. Sharma, S. K. Goel, Erosion behavior of WC–10Co–4Cr coating on 23-8-N nitronic steel by HVOF thermal spraying. Applied Surface Science **370** (2016): 418-426. https://doi.org/10.1016/j.apsusc.2016.02.163.

[20] Q. Wang, S. Luo, S. Wang, H. Wang, C. Seshadri Ramachandran, Wear, erosion and corrosion resistance of HVOF-sprayed WC and Cr_3C_2 based coatings for electrolytic hard chrome replacement, *International Journal of Refractory Metals and Hard Materials* **81** (2019) 242-252. https://doi.org/10.1016/j.ijrmhm.2019.03.010.

[21] A Kumar Singla, A. Bansal, V. Singh, N. Khanna, D. Kumar Goyal, J. Singla, Satish Tailor, Development, characterization, and cavitation erosion analysis of high velocity oxy-fuel (HVOF) sprayed TiC and (70Cu-30Ni)-Cr based composite coatings on SS316 steel, *Tribology International* **186** (2023) 108621. https://doi.org/10.1016/j.triboint.2023.108621

[22] V. Singh, A. Bansal, A. Kumar Singla, D. Kumar Goyal, N. Khanna, Modification of SS316 steel with the assistance of high velocity oxy fuel (HVOF) process to upsurge its sustainability, In *Sustainable Materials and Manufacturing Technologies*, . CRC Press, 2023. 182-195. https://doi.org/10.1201/9781003291961

[23] X. Liu, J. Kang, W. Yue, Z. Fu, L. Zhu, D. She, J. Liang, C. Wang, Performance evaluation of HVOF sprayed WC-10Co4Cr coatings under slurry erosion, *Surface Engineering,* **35** (2019) 816-825. https://doi.org/10.1080/02670844.2019.1568661.

[24] V. Singh, A. Kumar Singla, A. Bansal, Influence of TiC Content on Slurry Erosion Behaviour of HVOF Sprayed Titanium Carbide and Cupronickel-Chromium Based Coatings, *Journal of Thermal Spray Technology* **32** (2023) 1739-1757. https://doi.org/10.1007/s11666-023-01613-2.

[25] N. Kumar, N. Arora, S. K. Goel, Slurry erosion study on nitrogen-alloyed austenitic stainless steel and weld beads, *Tribology Letters* **68** (2020) 92. https://doi.org/10.1007/s11249-020-01332-7.

[26] A. K. Chauhan, D. B. Goel, S. Prakash, Erosive wear of a surface coated hydro turbine steel, *Bulletin of Materials Science* **33** (2010) 483-489. https://doi.org/10.1007/s12034-010-0074-0.

[27] A. Kumar, A. Sharma, S. K. Goel, Effect of heat treatment on microstructure, mechanical properties and erosion resistance of cast 23-8-N nitronic steel, *Materials Science and Engineering A* **637** (2015) 56-62. https://doi.org/10.1016/j.msea.2015.04.031.

[28] H. Myalska, K. Szymański, G. Moskal, Microstructure and selected properties of WC-Co-Cr coatings deposited by high-velocity thermal spray processes, *Solid State Phenomena* **246** (2016) 117-122. https://doi.org/10.4028/www.scientific.net/ssp.246.117.

[29] S. L. Liu, X. P. Zheng, G. Q. Geng, Influence of nano-WC–12Co powder addition in WC–10Co–4Cr AC-HVAF sprayed coatings on wear and erosion behaviour, *Wear* **269** (2010) 362-367. https://doi.org/10.1016/j.wear.2010.04.019.

[30] K. Torkashvand, V. Krishna Selpol, M. Gupta, S. Joshi, Influence of test conditions on sliding wear performance of high-velocity air fuel-sprayed WC–CoCr coatings, *Materials* **14** (2021) 3074. https://doi.org/10.3390/ma14113074.

[31] Q. Wang, S. Zhang, Y. Cheng, J. Xiang, X. Zhao, G. Yang, Wear and corrosion performance of WC-10Co4Cr coatings deposited by different HVOF and HVAF spraying processes, *Surface and Coatings Technology* **218** (2013) 127-136. https://doi.org/10.1016/j.surfcoat.2012.12.041.

[32] K. Ofelia Méndez-Medrano, C. Jesús Martínez-González, F. Alvarado-Hernández, O. Jiménez, Víctor Hugo Baltazar-Hernández, H. Ruiz-Luna, Microstructure and properties characterization of WC-Co-Cr thermal spray coatings, *Journal of Minerals and Materials Characterization and Engineering* **6** (2018) 482-497. https://doi.org/10.4236/jmmce.2018.64034.

[33] M. M. El Rayes, E. M. Sherif, H. S. Abdo, Comparative Study into Microstructural and Mechanical Characterization of HVOF-WC-Based Coatings, *Crystals* **12** (2022) 969. https://doi.org/10.3390/cryst12070969.

[34] D. Naha, S. Chatterjee, M. Ghosh, J. Dutta Majumdar, A. Majumdar, HVOF sprayed WCCocr coating on mild steel: microstructure and wear evaluation, *IOSR J. Appl. Phys.* **8** (2016) 47-56. https://doi.org/10.9790/4861-08114756.

[35] K. Fan, W. Jiang, V. Luiz, T. Gong, W. Feng, J. Ruiz-Hervias, P. Yao, Influence of WC Particle Size on the Mechanical Properties and Residual Stress of HVOF Thermally Sprayed WC–10Co–4Cr Coatings, *Materials* **15** (2022) 5537. https://doi.org/10.3390/ma15165537.

[36] L. Chang, W. Wang, D. Ma, J. Xie, Deposition effects and interface structure of HVOF-sprayed multimodal WC-CoCr coatings, *Journal of Materials Research* **38** (2023) 4345-4356. https://doi.org/10.1557/s43578-023-01147-x.

[37] A. Karimi, C. Verdon, G. Barbezat, Microstructure and hydro abrasive wear behaviour of high-velocity oxy-fuel thermally sprayed WC-Co (Cr) coatings, *Surface and Coatings Technology* **57** (1993) 81-89. https://doi.org/10.1016/0257-8972(93)90340-T.

[38] A. Garfias Bulnes, V. Albaladejo Fuentes, I. Garcia Cano, S. Dosta, Understanding the influence of high-velocity thermal spray techniques on the properties of different anti-wear WC-based coatings, *Coatings* **10** (2020) 1157. https://doi.org/10.3390/coatings10121157.

[39] Y. Y. Santana, L. JG Barbera-Sosa, J. Caro, E. S. Puchi-Cabrera, M. H. Staia, Mechanical properties and microstructure of WC–10Co–4Cr and WC–12Co thermal spray coatings deposited by HVOF, *Surface engineering* **24** (2008) 374-382. https://doi.org/10.1179/174329408X326380.

[40] D. Kumar Goyal, H. Singh, H. Kumar, V. Sahni, Slurry erosive wear evaluation of HVOF-spray Cr 2 O 3 coating on some turbine steels, *Journal of thermal spray technology* **21** (2012) 838-851. https://doi.org/10.1007/s11666-012-9795-5.

[41] M. Aminul Islam, T. Alam, Z. N. Farhat, A. Mohamed, A. Alfantazi, Effect of microstructure on the erosion behavior of carbon steel, *Wear* **332** (2015) 1080-1089. https://doi.org/10.1016/j.wear.2014.12.004.

[42] I. A. Maekai, G. A. Harmain, Influence of operating parameters on slurry erosion of stainless steel f6nm, *Tribology in Industry* **42** (2020) 236. https://doi.org/10.24874/ti.780.10.19.02.

[43] C. S. Ramesh, D. S. Devaraj, R. Keshavamurthy, B. R. Sridhar, Slurry erosive wear behaviour of thermally sprayed Inconel-718 coatings by APS process, *Wear* **271** (2011) 1365-1371. https://doi.org/10.1016/j.wear.2011.01.057.

[44] S. Bhandari, H. Singh, H. Kumar, V. Rastogi, Slurry erosion performance study of detonation gun-sprayed WC-10Co-4Cr coatings on CF8M steel under hydro-accelerated conditions, *Journal of thermal spray technology* **21** (2012) 1054-1064. https://doi.org/10.1007/s11666-012-9799-1.

[45] M. H. Buszko, A. K. Krella, An influence of factors of flow condition, particle and material properties on slurry erosion resistance, *Advances in Materials Science* **19** (2019) 28-53. https://doi.org/10.2478/adms-2019-0010.

[46] G. Santacruz, A. Shigueaki Takimi, F. Vannucchi de Camargo, C. Pérez Bergmann, Cristiano Fragassa, Comparative study of jet slurry erosion of martensitic stainless steel with tungsten carbide HVOF coating, *Metals* **9** (2019) 600. https://doi.org/10.3390/met9050600.

[47] J. Malik, I. H. Toor, W. H. Ahmed, Z. M. GaSEM, M. A. Habib, R. Ben-Mansour, and H. M. Badr, Evaluating the effect of hardness on erosion characteristics of aluminum and steels, *Journal of materials engineering and performance* **23** (2014) 2274-2282. https://doi.org/10.1007/s11665-014-1004-x

[48] J. Singh, Analysis on suitability of HVOF sprayed Ni-20Al, Ni-20Cr and Al-20Ti coatings in coal-ash slurry conditions using artificial neural network model, *Industrial Lubrication and Tribology* **71** (2019) 972-982. https://doi.org/10.1108/ILT-12-2018-0460.

[49] R. Kumar, S. Kumar, D. Mudgal, Silt erosion performance of high velocity oxy fuel-(HVOF) sprayed Al2O3–Cr2O3 composite coatings on turbine steel, *Industrial Lubrication and Tribology* **74** (2022) 572-579. https://doi.org/10.1108/ILT-08-2021-0346.

[50] J. Du, J. Zhang, J. Xiao, C. Zhang, Slurry erosion behavior of HVOF sprayed WC-12Co and Cr3C2-25NiCr coatings deposited on 16Cr5Ni stainless steel, *Surface Review and Letters* **27** (2020) 1950193. https://doi.org/10.1142/S0218625X19501932.

[51] H. S. Grewal, H. S. Arora, A. Agrawal, H. Singh, S. Mukherjee, Slurry erosion of thermal spray coatings: effect of sand concentration, *Procedia Engineering* **68** (2013) 484-490. https://doi.org/10.1016/j.proeng.2013.12.210.

[52] V. Singh, A. Kumar Singla, A. Bansal, Influence of laser texturing along with PTFE topcoat on slurry and cavitation erosion resistance of HVOF sprayed VC coating, *Surface and Coatings Technology* **470** (2023) 129858. https://doi.org/10.1016/j.surfcoat.2023.129858.

[53] S. Brioua, K. Belmokre, V. Debout, P. Jacquot, E. Conforto, S. Touzain, Jordi Creus, Corrosion behavior in artificial seawater of thermal-sprayed WC-CoCr coatings on mild steel by electrochemical impedance spectroscopy, *Journal of solid state electrochemistry* **16** (2012) 633-648. https://doi.org/10.1007/s10008-011-1403-y

[54] Y. Huang, X. Ding, C. Yuan, Z. Yu, Z. Ding, Slurry erosion behaviour and mechanism of HVOF sprayed micro-nano structured WC-CoCr coatings in NaCl medium, *Tribology International* **148** (2020) 106315. https://doi.org/10.1016/j.triboint.2020.106315.

[55] M. Sharma, D. Kumar Goyal, G. Kaushal, Tribological investigation of HVOF-sprayed coated turbine steel under varied slurry erosion conditions, Material proceedings **24** (2020) 869-879. https://doi.org/10.1016/j.matpr.2020.04.397.

[56] X. Liu, J. Kang, W. Yue, Z. Fu, L. Zhu, D. She, J. Liang, C. Wang, Performance evaluation of HVOF sprayed WC-10Co4Cr coatings under slurry erosion, *Surface Engineering* **35** (2019) 816-825. https://doi.org/10.1080/02670844.2019.1568661.

[57] D. C. Ribu, R. Rajesh, D. Thirumalaikumarasamy, A. R. Kaladgi, C. A. Saleel, K.S. Nisar, A. Afzal, Experimental investigation of erosion-corrosion performance and slurry erosion mechanism of HVOF sprayed WC-10Co coatings using design of experiment approach. Journal of Materials Research and Technology, **18** (2022), 293-314. https://doi.org/10.1016/j.jmrt.2022.01.134.

[58] E. Sadeghimeresht, N. Markocsan, P. Nylén, A comparative study of corrosion resistance for HVAF-sprayed Fe-and Co-based coatings, *Coatings* **6** (2016) 16. https://doi.org/10.3390/coatings6020016.

[59] T. Arunnellaiappan, S. Baskaran, S. Arun, R. Prithivirajan, Corrosion behaviour of detonation gun sprayed cermet coatings on AA5083, *Surface Engineering* **37** (2021) 263-270. https://doi.org/10.1080/02670844.2020.1807096.

[60] J. A. Picas, E. Rupérez, M. Punset, A. Forn, Influence of HVOF spraying parameters on the corrosion resistance of WC–CoCr coatings in strong acidic environment, *Surface and Coatings Technology* **225** (2013) 47-57. https://doi.org/10.1016/j.surfcoat.2013.03.015.

[61] F. Wang, F. Zhang, L. Zheng, H. Zhang, Structure and corrosion properties of Cr coating deposited on aerospace bearing steel, *Applied Surface Science* **423** (2017) 695-703. https://doi.org/10.1016/j.apsusc.2017.06.099.

[62] J. E. Cho, S. Y. Hwang, K. Y. Kim, Corrosion behavior of thermal sprayed WC cermet coatings having various metallic binders in strong acidic environment, *surface and coatings technology* **200** (2006) 2653-2662. https://doi.org/10.1016/j.surfcoat.2004.10.142.